MIT Libraries | DSpace@MIT

MIT Open Access Articles

Enabling Ideal Selective Solar Absorption with 2D Metallic Dielectric Photonic Crystals

The MIT Faculty has made this article openly available. ***Please share*** how this access benefits you. Your story matters.

Citation: Chou, Jeffrey B., Yi Xiang Yeng, Yoonkyung E. Lee, Andrej Lenert, Veronika Rinnerbauer, Ivan Celanovic, Marin Soljacic, Nicholas X. Fang, Evelyn N. Wang, and Sang-Gook Kim. "Enabling Ideal Selective Solar Absorption with 2D Metallic Dielectric Photonic Crystals." Advanced Materials (September 2014).

As Published: http://dx.doi.org/10.1002/adma.201403302

Publisher: Wiley Blackwell

Persistent URL: http://hdl.handle.net/1721.1/90486

Version: Author's final manuscript: final author's manuscript post peer review, without publisher's formatting or copy editing

Terms of use: Creative Commons Attribution-Noncommercial-Share Alike

Massachusetts Institute of Technology

DOI:
Article type: Communication

Enabling Ideal Selective Solar Absorption with 2D Metallic Dielectric Photonic Crystals

Jeffrey B. Chou, Yi Xiang Yeng, Yoonkyung E. Lee, Andrej Lenert, Veronika Rinnerbauer, Ivan Celanovic, Marin Soljačić, Nicholas X. Fang, Evelyn N. Wang, and Sang-Gook Kim**

Dr. J. B. Chou
Room 41-211
77 Massachusetts Ave, Cambridge MA, 02139, USA
E-mail: jeffchou@mit.edu

Prof. S.-G. Kim
Room 1-306
77 Massachusetts Ave, Cambridge MA, 02139, USA
E-mail: sangkim@mit.edu

Y. X. Yeng, Y.E. Lee, A. Lenert, Dr. I. Celanovic, Prof. M. Soljačić, Prof. N. X. Fang, Prof. E. N. Wang,
77 Massachusetts Ave, Cambridge MA, 02139, USA

Dr. V. Rinnerbauer
Altenbergerstraße 69, 4040 Linz, Austria

Keywords: absorber, solar, thermophotovoltaic, photonic crystal, cavity modes

The selective absorption of sunlight plays a critical role in solar-thermophotovoltaic (STPV) energy conversion by tailoring both the absorption and emission spectrums for efficient solar-thermal-electrical energy conversion. [1–7] By selectively absorbing solar energy while suppressing long wavelength emission, optimal solar-thermal energy conversion can be achieved. In practical STPV systems, selective absorbers must simultaneously contain optical, manufacturing, and reliability properties. Previous efforts have typically focused only on a subset of these requirements. In this communication, we present our solution which contains all of the ideal properties of a selective absorber for large-scale and efficient solar energy conversion.

The effective absorption of solar energy requires selective absorption across the solar spectrum, high temperature reliability, omnidirectional absorption, and wafer-scale fabrication

for mass scalability. Recent developments of metal based selective absorbers have demonstrated 1D, 2D, and 3D metallic photonic crystal structures capable of tailoring the absorption spectrum.[2,8–14] One dimensional metal dielectric stacks have demonstrated promising solar absorbing properties but are unstable at temperatures greater than approximately 600°C.[13] In particular, two-dimensional metallic air photonic crystals (MAPhC) have been shown to selectively absorb light in the near-IR via cavity modes and withstand high temperatures greater than 1000°C; however, the acceptance angle is limited to ±30°, and the absorption in the visible spectrum is limited due to diffraction.[2,11,15] Metamaterial and plasmonic based absorbers have demonstrated wide angle absorption due to their subwavelength periodic structures; however high temperature stability and wafer-scale fabrication have yet to be shown.[1,3,16–19]

Here we present our 2D metallic dielectric photonic crystal (MDPhC) structure, which simultaneously demonstrates broadband (visible to near-IR) absorption, omnidirectional absorption, wafer-scale fabrication, and high temperature robustness.[20] The wafer-scale fabricated MDPhC has a measured absorption of 85% for photon energies $5\ eV > \hbar\omega > 0.7\ eV$ and an absorption below 10% for $\hbar\omega < 0.4\ eV$. Angled measurements show existence of the cavity modes for angles up to 70° from normal. Furnace tests at 1000°C for 24 hours show a robust optical performance due to its fully encapsulated design which helps to retain the metal cavity shapes at high temperatures.[21] Finite-difference time-domain (FDTD) and rigorous coupled wave analysis (RCWA) based simulations indicate that the broadband absorption is due to a high density of hybrid cavity and surface plasmon modes overlaped with an anti-reflection coating (ARC).

A schematic image of the MDPhC is shown in **Figure 1**(a) and (b). The MDPhC utilizes cut-off frequencies of cavity modes to tailor the absorption. Since the cut-off frequency is dependent on the geometry of the cavities, the absorption spectrum can be tuned by simply modifying the radius and depth of the cavities.[2,22] Photos and SEM images of the

device are shown in Figure 1(c)-(f) where the multilayered structure was fabricated using the sidewall lithography technique across a 6” wafer (see supporting information).[23–25] An 80 nm thick layer of ruthenium is used as the metal, which was deposited via atomic layer deposition (ALD) for conformal deposition purposes. The dielectric filling of HfO_2 is also deposited via ALD, and excess HfO_2 is removed via chemical mechanical polishing (CMP). A layer of HfO_2 with a thickness of approximately $t = 25$ nm is left on top of the entire structure. HfO_2 is chosen due to its conformal deposition, high melting temperature, and transparency in the visible and infrared (IR) regime. The fully fabricated 6” wafer is shown in Figure 1(c), where it has been diced into 1 cm ×1 cm chips. An angled scanning electron microscope (SEM) image of the 70 nm thick Al_2O_3 shells before the metal is deposited is shown in Figure 1(d) and of the wafer after the CMP process in Figure 1(e). A cross section SEM image obtained via focused ion beam (FIB) milling is shown in Figure 1(f) which confirms the complete filling of the metallic cavities. Due to the large area nature of the fabrication, small variations of the material thicknesses are observed which explains the reason why Figure 1(e) and (f) are slightly different, however these small variations do not significantly impact the absorption spectrum (see supporting information). Along with the cut-off frequency, the design of the cavities is also based on Q-matching formalism where maximum absorption occurs when the radiative Q_{rad} and the absorption Q_{abs} are equal.[22,26]

The measured absorption spectrum shown in **Figure 2**(a), demonstrates the broadband absorption of the MDPhC across the majority of the solar spectrum along with a steep cut-off frequency. A UV-Vis-near-IR Cary 500i spherical diffuse reflectance measurement accessory was used to obtain the total absolute absorption spectrum ($\alpha_t = 1 - R_t - T_t$) of the MDPhC, MAPhC, and flat ruthenium at an incidence of 3° with unpolarized light. The terms R_t and T_t are the total reflection and transmission values. For absorption measurements at photon energies in the IR, a fourier transform infrared (FTIR) spectrometer was used with a commercial aluminium coated reference mirror. The FDTD simulated absorption of the

MDPhC layer agrees well with experiment, but diverges for $\hbar\omega > 3\ eV$, where transmission through the metal layer can no longer be assumed to be $T_t = 0$. At these frequencies, the silicon substrate absorbs the transmitted light. The cut-off frequency is located at mode M_1 with $\hbar\omega = 0.75\ eV$, below which the absorption is supressed to below 10% for $\hbar\omega < 0.4\ eV$.

In comparison, the MAPhC measured absorption spectrum is shown in Figure 2(b), which has a poorer absorption profile over the visible frequencies due to diffraction losses.[2,20] The MAPhC has the same dimensions as the MDPhC, however the MAPhC does not have the HfO_2 filling. The cut-off frequency for the MAPhC shifted by a factor of 2.07 to 1.55 eV, which closely matches the measured index of the HfO_2 in the cavity. The FDTD simulated MAPhC absorption is also shown which agrees well in frequency, but has higher absorption values than measured. Mismatch between the simulation and experiment may also be attributed to both the smooth cylindrical structure and perfect uniform geometry in the simulation that are not present in the actual device due to the large scale fabrication variation.

The broadband optical properties of the MDPhC in the visible regime are due to the combination of a high density of cavity modes and an ARC layer. The dielectric filling essentially red-shifts the frequencies of the high order cavity modes to create a high density of states in the visible regime. Experimentally, this can be observed in the larger number of peaks in the measured MDPhC absorption spectrum in comparison to the MAPhC absorption spectrum in Figure 2(a) and (b), respectively. The first two modes, M_1 and M_2, are standard cavity modes, however, the third mode, M_3 ($\hbar\omega = 2.21$ eV) supports a hybrid cavity and SPP mode as can be seen in the E_x field image in Figure 2(c). The coupling between cavity and SPP modes may also contribute to the increased absorption in the M_3 mode.[27]

The wavelength of mode M_3 ($\lambda_3 = 560$ nm) occurs at wavelengths below the period of the MDPhC ($a = 780$ nm) where diffraction losses typically occur. Thus, an ARC layer serves to minimize reflections at the top surface of the MDPhC and increase the absorption in the visible spectrum. To demonstrate this, Figure 2(d) shows absorption spectra of the

MDPhC with and without an ARC layer; the spectrum with an ARC layer shows considerably higher absorption at the M_3 mode than without an ARC layer. Figure 2(e) shows the intensity plots of the M_3 mode with a reduced reflected intensity at the top metal surface due to destructive interference caused by the ARC layer in comparison to the same mode without an ARC layer shown in Figure 2(f). Furthermore, integration of the FDTD simulated Poynting vector reveals that the ARC layer causes 44% of the incident light power to be absorbed at the top metal surface for mode M_3, whereas without an ARC layer only 33% is absorbed.

Analytically, the ARC layer on a flat HfO_2 and ruthenium interface can be calculated by inserting the complex permittivity of the metal (ϵ_{Ru}) layer into the Fresnel reflection equation.[28] To suppress undesired reflection in the visible spectrum of $\hbar\omega = 1.55$ eV → 3.1 eV, with an average index of HfO_2 at in the visible regime of $n = 2.09$, we calculate an ARC layer thickness of $t_{ARC} = 22$ nm → 72 nm for a flat surface. Thus, if the proper ARC layer thickness is designed to spectrally overlap with the high density of optical states, high, broadband absorption will occur.

To verify the wide angle absorption properties and high temperature stability of the MDPhC, the measured spectra at various angles are shown in **Figure 3**. As previously explained, the dielectric filling in the MDPhC down-shifts the frequency of the low order modes to be below the diffraction threshold thus improving the wide angle absorption.[20] Clearly the cavity modes in Figure 3(a) remain relatively fixed in frequency as a function of angle, which is a characteristic of the cavity modes. RCWA simulations of the MDPhC absorption at incident angles up to 90° are shown in Figure 3(b) and agree well with the experimentally measured absorption spectrum in Figure 3(a).[29] An incident planewave with both S and P polarizations is used. The simulated average absorption for wavelengths from 2.76 eV to 0.69 eV and incident angle from 0° to 70° is 0.72. Angular dependence of the higher order absorption modes is due to diffraction effects via Wood's anomaly and ARC angle dependence.[30]

The same MDPhC sample measured in Figure 3(a) was then placed in a furnace at 1000°C for 24 hours in a 95% Ar and 5% H_2 environment and re-measured again as shown in Figure 3(c) where the cut-off absorption peaks remain high, thus demonstrating the high temperature structural robustness of the MDPhC.[21] An approximate ≈8% drop in absorption is observed at higher frequencies above 3 eV due to the surface diffusion of the structure. The homologous temperatures of the furnace test for ruthenium, HfO_2, and Al_2O_3 are $T_{H,Ru} = 0.49$, $T_{H,HfO_2} = 0.42$, and $T_{H,Al_2O_3} = 0.54$, respectively, where diffusion effects are typically expected to be observed. SEM images of the ARC covered areas before and after the furnace test shown in Figure 3(d) and (e), respectively, show no physical damage on the top surface. However, SEM images of areas with no ARC layer before and after the furnace test shown in Figure 3(f) and (g), respectively, show extensive surface diffusion and detachment of the ruthenium from the HfO_2.

A FIB cross section image of a post-furnace ARC area is shown in Figure 3(h), where detachment and surface diffusion of the Ru are still observed underneath the ARC coating for roughly 50% of the cavities. We suspect that the poor adhesion between the Ru and HfO_2 caused the delamination between the two materials during the heating and cooling of the chip. The delamination then allowed for substantial surface diffusion of Ru. The top ARC coating does prevent the Ru from diffusing up and out of the plane of the MDPhC, as seen in Figure 3(g), thus reducing one of the diffusion paths and increasing the survivability of the cavities. If the delamination between the metal and dielectric layers can be prevented via improved adhesion between the layers, then surface diffusion of the metal structures with small radii of curvatures may be suppressed.[21] Furthur study of possible adhesion layers, such as TiN, is underway to prevent delamination at higher temperatures and to test the suppressed surface diffusion.[14] Despite the surface diffusion of Ru, the HfO_2, and Al_2O_3 act as a mold to retain the shape of the metallic cavities during the diffusion process. As a result, the cavity modes remain in the post-furnace absorption spectrum, showing the robustness of the cavity modes

to altered geometries due to high temperature effects. ARC samples were also placed under solar concentrated (259.11×±11.23 at 25.9 W/cm^2) light for 1 minute long on/off pulses for up to 10 iterations reaching temperatures up to 900°C measured via a bonded thermocouple and showed no sign of physical degradation.

In conclusion, we experimentally demonstrate a solar broadband, wide angle, high temperature stable and wafer-scale fabricated solar absorber. The MDPhC presented here is well suited for solar absorbing applications involving high levels of diffuse, optical concetration, and high temperatures. We demonstrate that fully encapsulated metal in dielectric is beneficial for high temperature robustness. Furthermore, absorption of the entire solar spectrum on a single layer metal surfaces in the MDPhC, allows for ultra-thin absorbers, further extending applications into flexible absorbers/emitters, photoelectrolysis, and hot-electron generation.[31,32] The wafer-scale fabricated compatibility of the MDPhC will lead to low-cost and mass producible next-generation solar energy converting devices. The MDPhC structure may be designed with various alternative metals and dielectrics to suit any application's needs. Although the selection of ALD depositable metals is limited, we experimentally confirmed that sputtered deposition of tungsten had similar conformal coverage, thus drastically expanding the selection of metals. With further optimization of the structure and materials, MDPhCs could play a critical role in the future of solar energy conversion.

Experimental Section

Absorption Measurements

The absolute reflection was measured with a commercial diffuse reference (Labsphere diffuse reflectance standard) with its own known reflection spectrum. An FTIR was used to measure the specular reflection from the wavelength range 1µm to 4 µm. A commercial reference aluminum coated mirror (Thorlabs) was used as the reference with its own known

reflection spectrum at angles 30°, 45°, 50°, 60°, and 70°. In both reflection measurements the optical source was an unpolarized broadband source.

FDTD Simulations

A commercial-grade simulator based on the finite-difference time-domain method was used to perform the calculations.[33] A Drude-Lorentz model of the metal was obtained by fitting room temperature measured reflection spectra of ALD deposited ruthenium as shown in Figure 2(a). The dielectric HfO_2 was modeled with a complex permittivity modeled based on measured ALD deposited HfO_2, with a long wavelength index of n=2.04. Absorption in the HfO_2 was experimentally measured to be zero for photon energies 4.96 eV and below. The optical source is a Gaussian distributed broadband pulse. The absorption spectra were simulated with an E_x polarized plane wave at normal incidence. The Al_2O_3 was modeled as a lossless dielectric with index n=1.5. The simulated total transmission, T_t, through the MDPhC is shown to verify that the MDPhC is in fact absorbing the majority of the input light.

RCWA Simulations

The metal is modelled with a complex permittivity, identical to the model used in the FDTD simulation. The HfO_2 is modelled as a lossless dielectric with constant index n=2.04. The dimensions used are identical to those in the FDTD simulation. A total number of 125 Fourier expansion orders are used for each spectrum.

Supporting Information

Supporting Information is available from the Wiley Online Library or from the author.

Acknowledgements

This work is supported as part of the Solid-State Solar Thermal Energy Conversion (S3TEC) Center, an Energy Frontier Research Center funded by the US Department of Energy, Office of Science, Office of Basic Energy Sciences under DE-FG02-09ER46577. Authors would like to thank Daniel Peykov and Walker R. Chan for their insightful discussions. The manuscript was written through contributions of all authors. All authors have given approval to the final version of the manuscript.

References

[1] T. V. Teperik, F. J. García de Abajo, A. G. Borisov, M. Abdelsalam, P. N. Bartlett, Y. Sugawara, J. J. Baumberg, *Nat. Photonics* **2008**, *2*, 299.
[2] Y. X. Yeng, M. Ghebrebrhan, P. Bermel, W. R. Chan, J. D. Joannopoulos, M. Soljačić, I. Celanovic, *Proc. Natl. Acad. Sci.* **2012**, *109*, 2280.
[3] C. Wu, B. N. Iii, J. John, A. Milder, B. Zollars, S. Savoy, G. Shvets, *J. Opt.* **2012**, *14*, 024005.
[4] S. Y. Lin, J. G. Fleming, D. L. Hetherington, B. K. Smith, R. Biswas, K. M. Ho, M. M. Sigalas, W. Zubrzycki, S. R. Kurtz, J. Bur, *Nature* **1998**, *394*, 251.
[5] A. Lenert, D. M. Bierman, Y. Nam, W. R. Chan, I. Celanović, M. Soljačić, E. N. Wang, *Nat. Nanotechnol.* **2014**, *9*, 126.
[6] Y. Nam, Y. X. Yeng, A. Lenert, P. Bermel, I. Celanovic, M. Soljačić, E. N. Wang, *Sol. Energy Mater. Sol. Cells* **2014**, *122*, 287.
[7] V. Rinnerbauer, A. Lenert, D. M. Bierman, Y. X. Yeng, W. R. Chan, R. D. Geil, J. J. Senkevich, J. D. Joannopoulos, E. N. Wang, M. Soljačić, I. Celanovic, *Adv. Energy Mater.* **2014**, n/a.
[8] H. Sai, H. Yugami, Y. Kanamori, K. Hane, *Sol. Energy Mater. Sol. Cells* **2003**, *79*, 35.
[9] F. O'Sullivan, I. Celanovic, N. Jovanovic, J. Kassakian, S. Akiyama, K. Wada, *J. Appl. Phys.* **2005**, *97*, 033529.
[10] S. Y. Lin, J. Moreno, J. G. Fleming, *Appl. Phys. Lett.* **2003**, *83*, 380.
[11] V. Rinnerbauer, S. Ndao, Y. Xiang Yeng, J. J. Senkevich, K. F. Jensen, J. D. Joannopoulos, M. Soljacic, I. Celanovic, R. D. Geil, *J. Vac. Sci. Technol. B Microelectron. Nanometer Struct.* **2013**, *31*, 011802.
[12] K. A. Arpin, M. D. Losego, A. N. Cloud, H. Ning, J. Mallek, N. P. Sergeant, L. Zhu, Z. Yu, B. Kalanyan, G. N. Parsons, G. S. Girolami, J. R. Abelson, S. Fan, P. V. Braun, *Nat. Commun.* **2013**, *4*, DOI 10.1038/ncomms3630.
[13] C. E. Kennedy, *Review of Mid- to High-Temperature Solar Selective Absorber Materials*, National Renewable Energy Lab., Golden, CO. (US), **2002**.
[14] J. G. Fleming, S. Y. Lin, I. El-Kady, R. Biswas, K. M. Ho, *Nature* **2002**, *417*, 52.
[15] A. Gombert, in *AIP Conf. Proc.*, AIP Publishing, **2003**, pp. 123–131.
[16] K. Aydin, V. E. Ferry, R. M. Briggs, H. A. Atwater, *Nat. Commun.* **2011**, *2*, 517.
[17] X. Liu, T. Tyler, T. Starr, A. F. Starr, N. M. Jokerst, W. J. Padilla, *Phys. Rev. Lett.* **2011**, *107*, 045901.
[18] Y. Cui, K. H. Fung, J. Xu, H. Ma, Y. Jin, S. He, N. X. Fang, *Nano Lett.* **2012**, *12*, 1443.
[19] C. M. Watts, X. Liu, W. J. Padilla, *Adv. Mater.* **2012**, *24*, OP98.

[20] J. B. Chou, Y. X. Yeng, A. Lenert, V. Rinnerbauer, I. Celanovic, M. Soljačić, E. N. Wang, S.-G. Kim, *Opt. Express* **2014**, *22*, A144.
[21] H.-J. Lee, K. Smyth, S. Bathurst, J. Chou, M. Ghebrebrhan, J. Joannopoulos, N. Saka, S.-G. Kim, *Appl. Phys. Lett.* **2013**, *102*, 241904.
[22] M. Ghebrebrhan, P. Bermel, Y. X. Yeng, I. Celanovic, M. Soljačić, J. D. Joannopoulos, *Phys. Rev. A* **2011**, *83*, 033810.
[23] T. J. Seok, A. Jamshidi, M. Eggleston, M. C. Wu, *Opt. Express* **2013**, *21*, 16561.
[24] X. Liu, X. Deng, P. Sciortino, M. Buonanno, F. Walters, R. Varghese, J. Bacon, L. Chen, N. O'Brie, J. J. Wang, *Nano Lett.* **2006**, *6*, 2723.
[25] Y.-K. Choi, T.-J. King, C. Hu, *IEEE Trans. Electron Devices* **2002**, *49*, 436.
[26] Jeffrey Chou, K. Smyth, Sang-Gook Kim, Bellevue Washington, **2013**, pp. 576–577.
[27] D. Chanda, K. Shigeta, T. Truong, E. Lui, A. Mihi, M. Schulmerich, P. V. Braun, R. Bhargava, J. A. Rogers, *Nat. Commun.* **2011**, *2*, 479.
[28] K. C. Park, *Appl. Opt.* **1964**, *3*, 877.
[29] V. Liu, S. Fan, *Comput. Phys. Commun.* **2012**, *183*, 2233.
[30] R. W. Wood, *Phys. Rev.* **1935**, *48*, 928.
[31] C. Clavero, *Nat. Photonics* **2014**, *8*, 95.
[32] E. Knoesel, A. Hotzel, M. Wolf, *Phys. Rev. B* **1998**, *57*, 12812.
[33] *Lumerical Solutions, Inc.*, **n.d.**
[34] D. S. Y. Hsu, N. H. Turner, K. W. Pierson, V. A. Shamamian, *J. Vac. Sci. Technol. B Microelectron. Nanometer Struct.* **1992**, *10*, 2251.

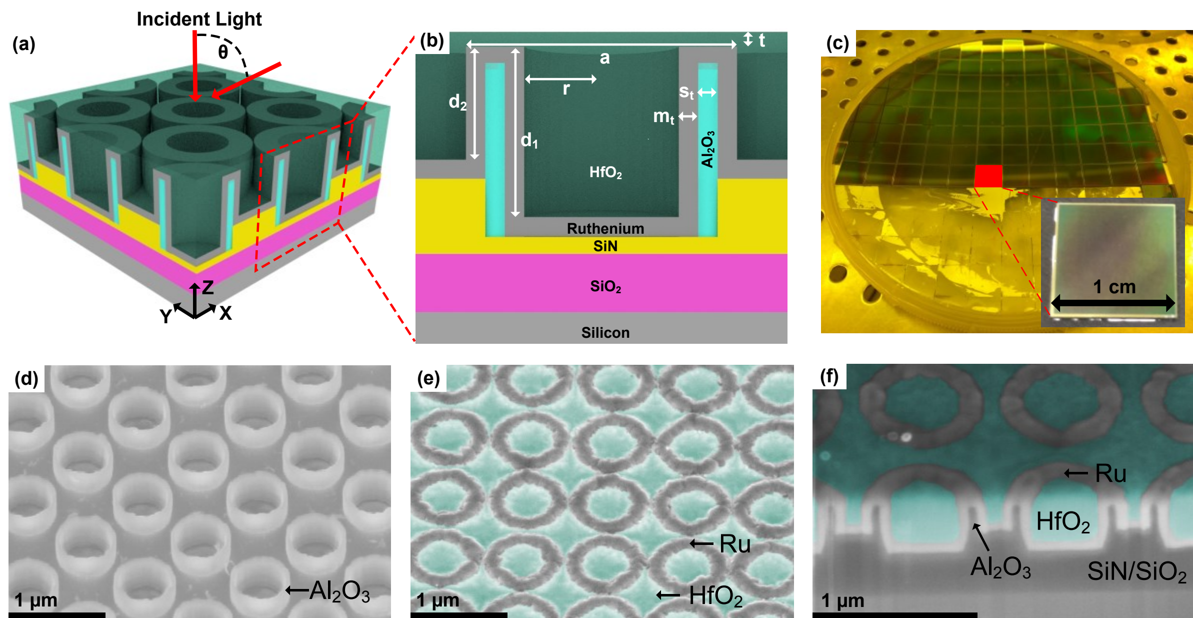

Figure 1. MDPhC images. (a) Schematic diagram of the MDPhC. (b) Schematic of the cross-section of the MDPhC with period *a,* radius *r*, depths d_1, d_2, metal thickness m_t, Al_2O_3 thickness s_t, and ARC thickness *t*. The HfO_2 filling has been made transparent for clarity. (c) Photo of the fully fabricated 6" wafer. (d) SEM image of the 40 nm thick Al_2O_3 shells before metallization. (e) SEM image of the fully fabricated wafer surface. (f) SEM image of the cross-section of the MDPhC taken at a 42° angle. Measured dimensions are $a = 790$ nm, $r = 200$ nm, $d_1 = 380$ nm, $d_2 = 200$ nm, $m_t = 80$ nm, $s_t = 40$ nm, and t is estimated to be approximately $t = 25$ nm.

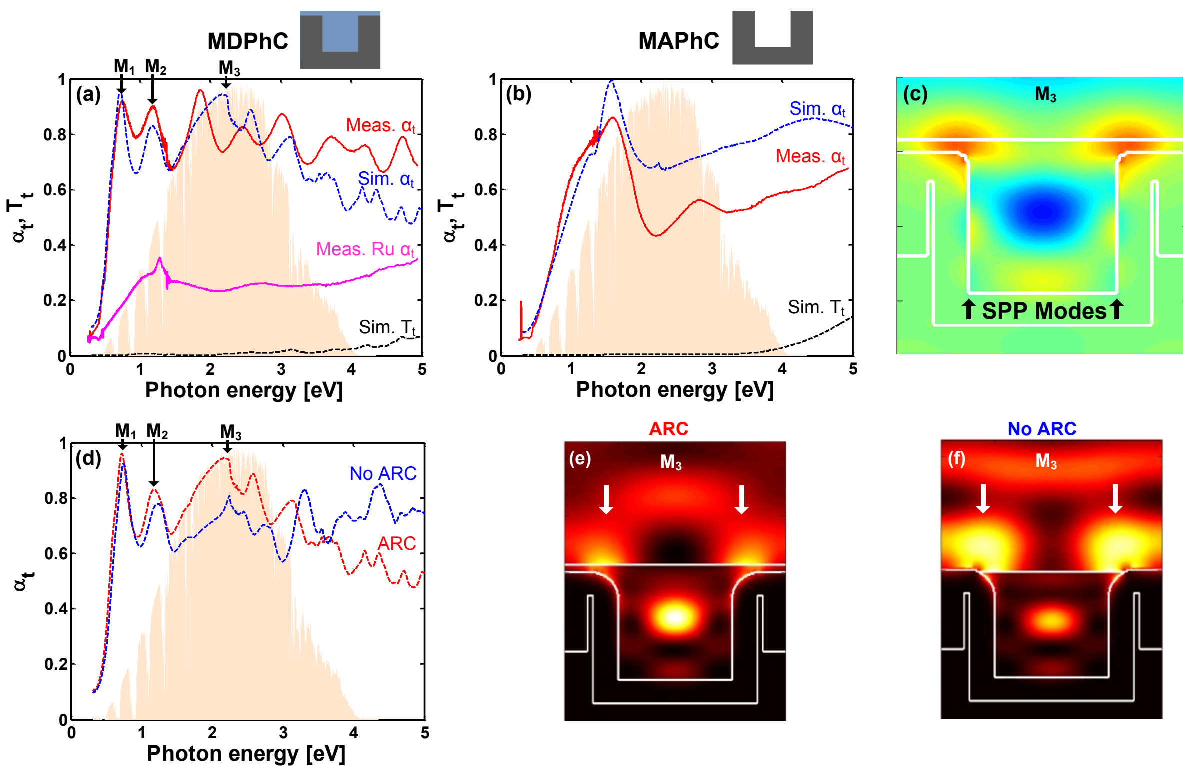

Figure 2. Absorption spectra. The total measured and simulated absorption spectrum for the (a) MDPhC and (b) MAPhC. An absorption measurement for flat ruthenium and the AM1.5 solar spectrum are shown for reference. The first three modes of the simulated spectrum are

labeled as M_1, M_2, and M_3 for reference. The FDTD simulated absorption and transmission spectra used structures with dimensions of $a = 780$ nm, $r = 200$ nm, $d_1 = 380$ nm, $d_2 = 200$ nm, $m_t = 80$ nm, $s_t = 40$ nm, and $t = 25$ nm. (c) E_x field image of the M_3 mode. SPP modes can be seen propagating along the vertical sidewalls of the cavity at the HfO_2/Ru interface. (d) Simulated absorption spectrum comparing MDPhCs with and without ARC coating. Simulations of the M_3 mode intensity $|E|^2$ plot are shown (e) with and (f) without the ARC layer. The intensity plot with an ARC layer has a reduced reflection intensity at the top metal surface indicated by the white arrows due to destructive interference.

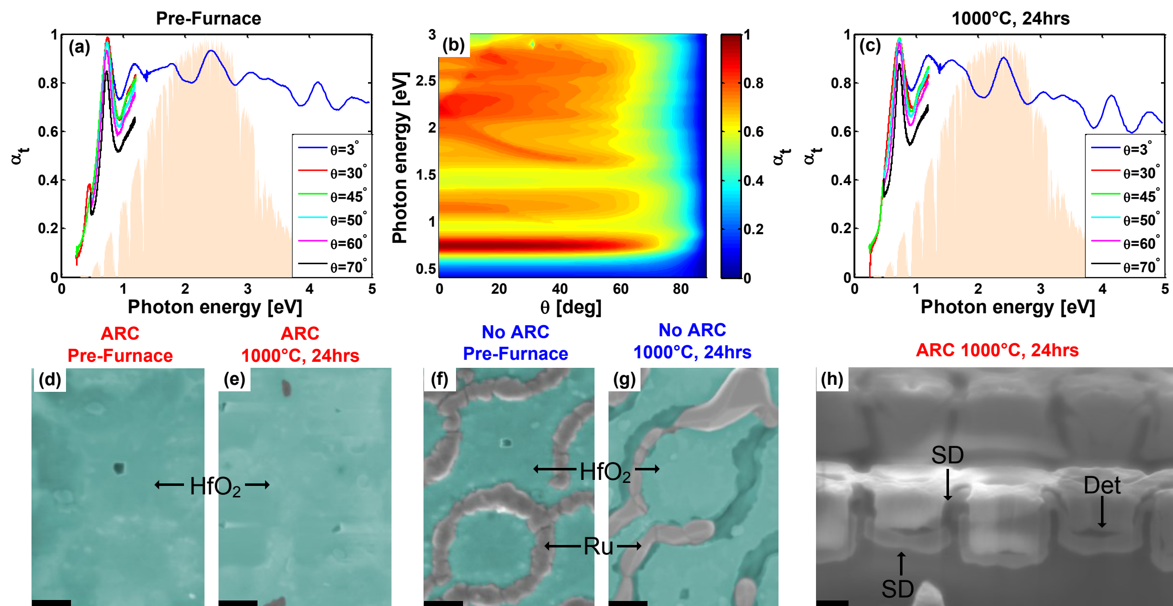

Figure 3. Wide-Angle and high temperature analysis of the MDPhC. (a) Measured absorption spectra at various angles at room temperature, prior to the furnace test. (b) Contour plot of the RCWA simulated absorption spectrum as a function of incident angle θ. (c) Measured absorption spectra after the 1000°C 24hr furnace test with the same sample showed in (a). SEM images of the ARC sample (d) before and (e) after the furnace test. Note, that due to the ARC layer the metal rings are no longer visible. SEM images of the non-ARC sample (f) before and (g) after furnace test. (h) SEM of the FIB cross section of the ARC sample after the furnace test. Degradation due to surface diffusion (SD) and detachment (Det) of the metal are indicated. All scale bars are 200 nm.

A metallic dielectric photonic crystal with solar broadband, omni-directional, and tunable selective absorption with high temperature stable (1000°C, 24 hrs) properties is fabricated on a 6” silicon wafer. The broadband absorption is due to a high density of optical cavity modes overlapped with an anti-reflection coating. Results allow for large-scale, low cost, and efficient solar-thermal energy conversion.

Keywords: absorber, solar, thermophotovoltaic, photonic crystal, cavity modes

Jeffrey B. Chou, Yi Xiang Yeng, Yoonkyung E. Lee, Andrej Lenert, Veronika Rinnerbauer, Ivan Celanovic, Marin Soljačić, Nicholas X. Fang, Evelyn N. Wang, and Sang-Gook Kim**

Enabling Ideal Selective Solar Absorption with 2D Metallic Dielectric Photonic Crystals

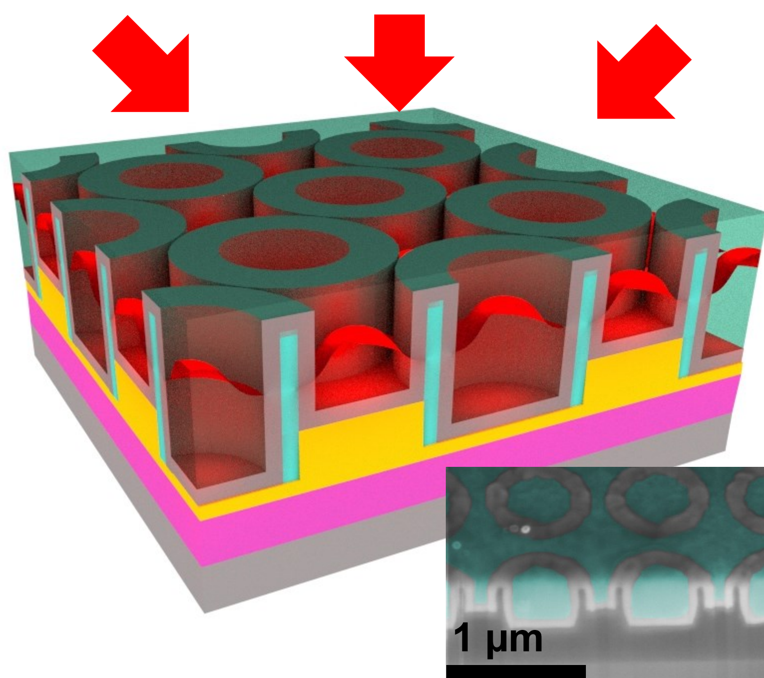

Copyright WILEY-VCH Verlag GmbH & Co. KGaA, 69469 Weinheim, Germany, 2013.

Supporting Information

Enabling Ideal Selective Solar Absorption with 2D Metallic Dielectric Photonic Crystals

Jeffrey B. Chou, Yi Xiang Yeng, Yoonkyung E. Lee, Andrej Lenert, Veronika Rinnerbauer, Ivan Celanovic, Marin Soljačić, Nicholas X. Fang, Evelyn N. Wang, and Sang-Gook Kim**

Wafer-Scale Fabrication

The fabrication process begins on a 6" silicon wafer cleaned with the RCA process. To prevent metal diffusion and eutectic mixing of the metal with the silicon at high temperatures, a diffusion barrier layer is deposited consisting of approximately 100 nm of thermal oxide followed by 150 nm of SiN deposited by low pressure chemical vapor deposition (LPCVD), as shown in **Figure S1**(a). A sacrificial 500 nm thick Poly Si layer is then deposited via LPCVD and patterned via an optical stepper with center wavelength of 369 nm. The photo-mask consists of a square checkerboard pattern with square dimensions of 0.6 µm × 0.6 µm. Due to the resolution limit of the stepper, the square pattern resolved to circles on the developed photoresist with a minimum inter-circle spacing of 200 nm, which is smaller than the wavelength of light used. The Poly Si layer is then etched via an SF_6 based RIE etch as shown in Figure S1(b). To remove any undesired debris on the surface, the photoresist is then removed via an ashing process, followed by a piranha and RCA clean. In Figure S1(c) 40 nm of Al_2O_3 is conformally deposited via atomic layer deposition (ALD) and anisotropically etched via a $Cl_2 + BCl_3$ based reactive ion etch (RIE) leaving only the sidewalls left. Since Cl_2 also etches Poly Si and SiN, both the Poly Si and SiN layers are slightly etched. The etching of the SiN layer causes the depths of the cavities to vary for inside and outside the metal cylinders. In Figure S1(d), a XeF_2 gas phased etch is used to etch the Poly Si only, thus leaving free-standing Al_2O_3 cylindrical shells on the wafer surface.[23,24,34] Next, in Figure S1(e), approximately 80 nm of ruthenium was deposited via

ALD over the Al_2O_3 shells. Finally, in Figure S1(f), a 36-hour ALD deposition of HfO_2 was used to fill up the cavities. To remove the excess HfO_2 on top of the wafer, a 15 minute chemical mechanical polishing (CMP) step was used. Due to the non-uniformity of the CMP process, a gradient of top HfO_2 thickness remained on the surface of the wafer from approximately 0 nm to 50 nm. The 6" wafer was then diced into 1 cm × 1 cm pieces. An annealing step of 1000°C for 24 hours in an inert environment (95% Ar, 5% H_2) has been shown to improve the optical absorption spectrum by removing undesired gap modes and increase absorption.

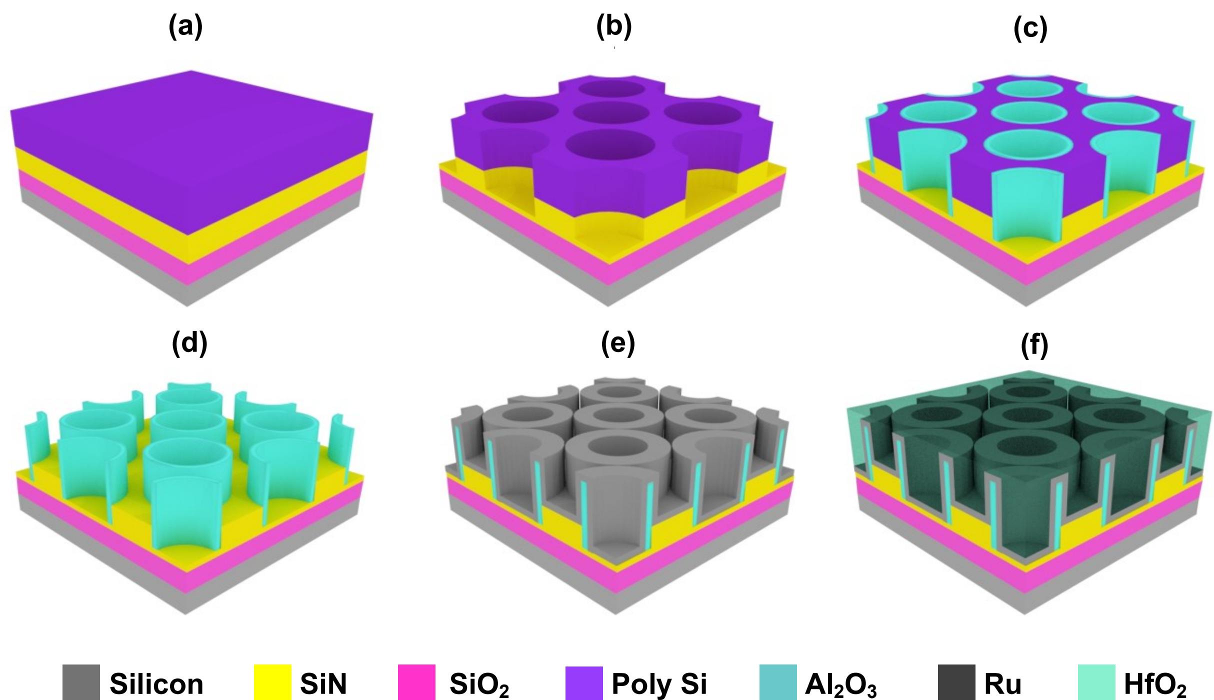

Figure S1. Wafer-scale fabrication schematic. (a) Six inch wafer with 100 nm of thermal SiO2, 150 nm of SiN, and 500 nm of poly Si deposited via LPCVD. (b) Poly Si layer is patterned with a UV stepper and etched with RIE. The SiN layer is etched due to overetching. (c) 40 nm of Al_2O_3 is conformally deposited via ALD then anisotropically etched via RIE to leave only the sidewalls remaining. (d) Poly Si layer is etched via XeF_2 gas etch leaving only the AL_2O_3 sidewalls, as shown in Figure 1(d). (e) 80 nm of Ruthenium is deposited via ALD. (f) HfO_2 is deposited via ALD for 36 hrs to fill the cavities and polished with CMP for 15 min to expose the metal dielectric interface, as shown in Figure 1(e).

Images of the device during and after fabrication are shown in **Figure S2**. In Figure S2(a) the photoresist is patterned with a square checkerboard photomask with a period 0.6 μm.

An inter-hole spacing of 200 nm is achieved via a combination of exposure time and photoresist developing overetch. In Figure S2(b) the sidewalls of Al_2O_3 are shown, which also shows the near 90° etch profile of the Poly Si trenches, which is critical for the sidewall lithography process. In Figure S2(c), the Poly Si is removed via XeF_2, which has almost perfect selectivity to Al_2O_3, which makes it an ideal sacrificial layer. In Figure S2(d), approximately 80 nm of ruthenium is conformally deposited across the wafer via ALD. A gradient of HfO_2 layer thickness occurred across the wafer leaving certain chips with a thin HfO_2 layer, Figure S2(e), and others without a thin HfO_2 layer, Figure S2(f).

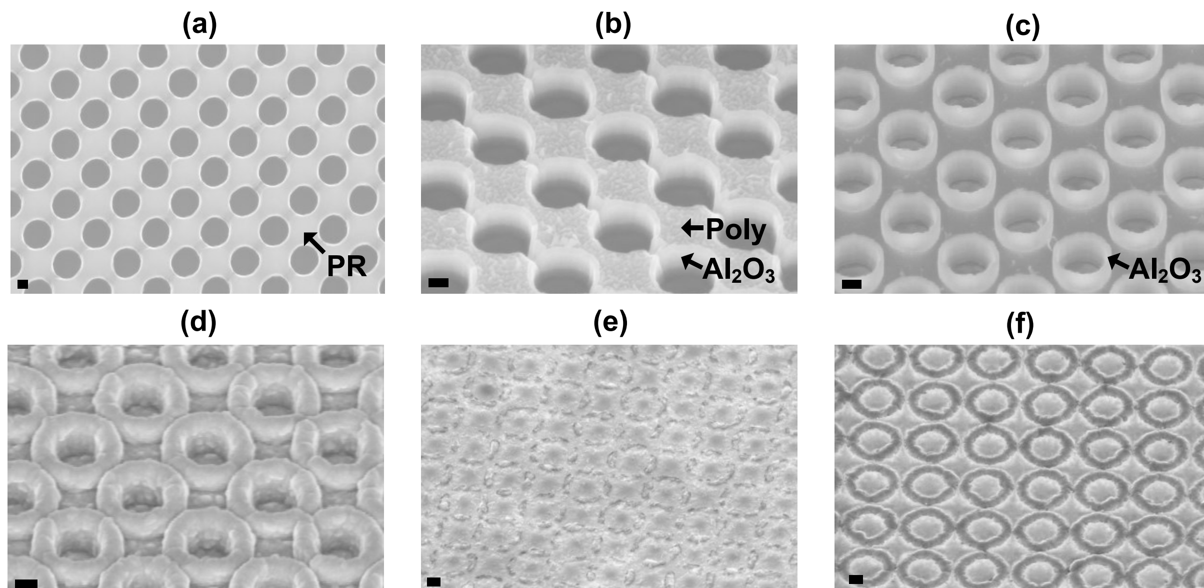

Figure S2. SEM images during and after the fabrication process. All scale bars are 200 nm. (a) Image of the patterned photoresist (PR) with inter hole spacing of 200 nm. (b) Image of the Poly Si and etched Al2O3 sidewalls, corresponding to Figure S1(c). (c) The 40 nm thick Al_2O_3 cylindrical shells after the XeF_2 etch, corresponding to Figure S1(d). (d) Image after the 80 nm thick ruthenium ALD deposition, corresponding to Figure S1(e). (e) Image of the completed device after the CMP process with a thin HfO_2 layer remaining on the top surface. (f) Image of the completed device with no HfO_2 layer remaining on the top surface. Here, the conductive metal surface is clearly visible.

Initially ALD was chosen for the metal deposition to ensure conformal coverage of the metal, however, we also experimentally confirmed that sputtering is also equally conformal for these structures, which allows for a wider variety of metals to be deposited. In **Figure S3**,

an SEM image of a tungsten sputtered MAPhC is shown, which clearly shows conformal coverage comparable to ALD. For cavities with higher depth to diameter aspect ratios, sputtering may not be useful due to its non-conformal coverage.

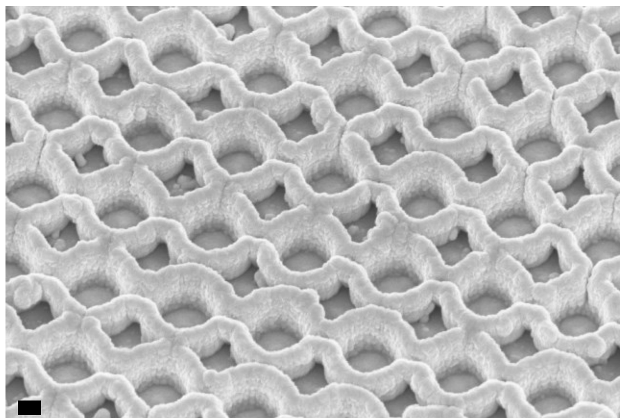

Figure S3. SEM image of a tungsten sputtered on the Al_2O_3 shells, as in Figure 2(e). Sputtered metal allows for a wide variety of materials to be used. Scale bar is 200 nm.

ARC Layer Analaysis

For a more detailed analysis, the ARC layer is varied in **Figure S4**. As the ARC layer increases in thickness, the overlap between the cavity modes and the ARC layer reflection spectrum red shifts. Thus, based on the application, different absorption spectra can be obtained by simply varying the ARC layer. A global optimization of the cavity geometry, ARC layer thickness, material thicknesses, and materials could be performed to create a more ideal absorption profile. The high sensitivity of ARC layer on the absorption spectrum could also be used for biological or chemical sensing applications.

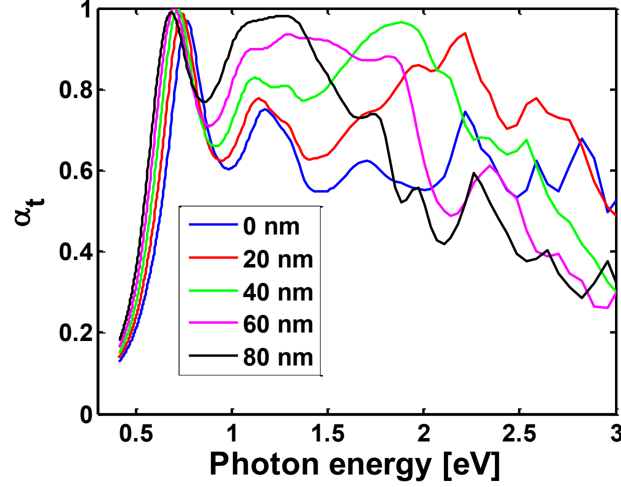

Figure S4. RCWA simulated absorption spectra for varied ARC thicknesses.

The ARC layer thickness t_{ARC} for a particular wavelength λ can be analytically calculated for the HfO_2/ruthenium interface:[28]

$$t_{ARC} = \frac{\lambda}{4\pi n}\left(2\pi - \operatorname{atan}\left(\frac{\Gamma''}{\Gamma'}\right)\right) \tag{1}$$

Where t_{ARC} is the ARC layer thickness, λ is the free-space wavelength, n is the index of the ARC layer, and Γ' and Γ'' are the real and imaginary components of the reflectivity at the HfO_2 and ruthenium interface defined by

$$\Gamma = \frac{n - \sqrt{\epsilon_{Ru}}}{n + \sqrt{\epsilon_{Ru}}} = \Gamma' + j\Gamma'' \tag{2}$$

Where ϵ_{Ru} is the complex permittivity of ruthenium. We note that the positive angle form should be used in the atan calculation in Eq. 1.

Cavity Modes

The simulated E_x field images are shown in **Figure S5** for the first 5 modes. The first two modes are standard cavity modes with to coupling to SPP modes. Modes M_3 and M_4 show both cavity and SPP modes, where the SPP modes are propagating along the vertical sidewalls of the cavity. Mode M_5 shows a high order cavity mode with little coupling to SPP

modes. The higher order modes appear to be dominated by cavity modes and are what cause the high density of optical states in the visible regime.

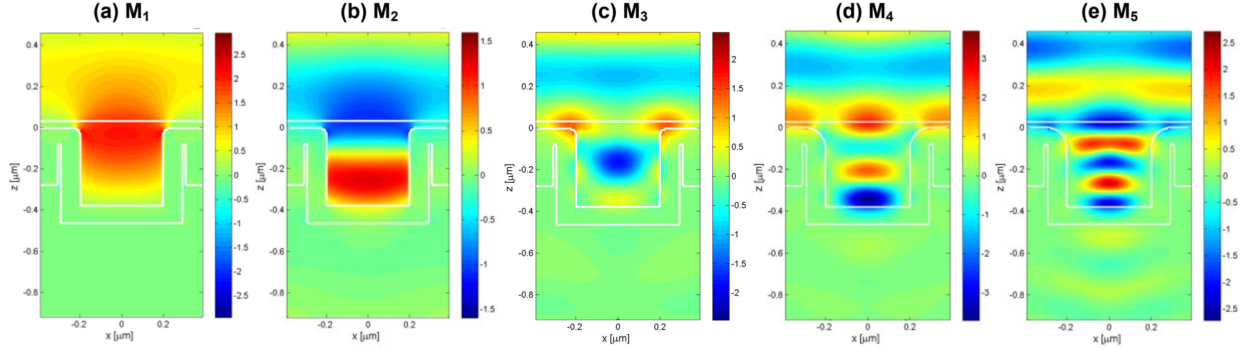

Figure S5. Simulated E_x field images of the first 5 modes in the MDPhC absorption spectrum. Modes M_1 and M_2 are standard cavity modes with no coupling to SPP modes. Modes M_4 and M_5 correspond to the simulated absorption peaks at photon energies $\hbar\omega = 2.55$ eV and 3.17 eV, respectively.

Effect of metal (m_t) and Al_2O_3 (s_t) thickness

The effect of metal thickness, m_t, on the absorption spectrum of the MDPhC is shown in **Figure S6**, where both the metal, m_t, and Al_2O_3, s_t, thicknesses are varied to keep the inner radius, r, constant. For m_t greater than the skin depth, the absorption spectra remains relatively constant, as seen for $m_t > 50\ nm$. In this regime, the thickness of the Al_2O_3 has no impact on the absorption spectra since the fields do not significantly penetrate the metal. Once the metal thickness is below the skin depth, as shown for $m_t = 25\ nm$, the transmission of the fields through the metal lowers the absorption spectra. In this regime, the thickness of the Al_2O_3 can alter the absorption spectra by allowing for modes within the Al_2O_3 to occur. However, the fabricated MDPhC presented in this communication has metal thickness greater than the skin depth, and as a result the Al_2O_3 thickness has little effect on the absorption spectrum. Therefore, although the Al_2O_3 thickness varies across the wafer by approximately 40 nm - 80 nm, due to non-uniform deposition and etching processes, this variation does not impact the absorption spectrum. Furthermore, variations in the metal thickness across the

wafer also do not have a significant impact on the absorption spectrum, since the minimum observed metal thicknesses is approximately 70 nm. In summary, as long as the metal thickness is greater than the skin depth, the absorption spectra is immune to small variations in metal or Al_2O_3 thicknesses. We comment that this analysis assumes that the inner radius, *r*, remains constant. If variations of the metal or Al_2O_3 thickness change the inner radius, *r*, then the frequency of the modes will red shift or blue shift depending on the direction of the change in *r*.

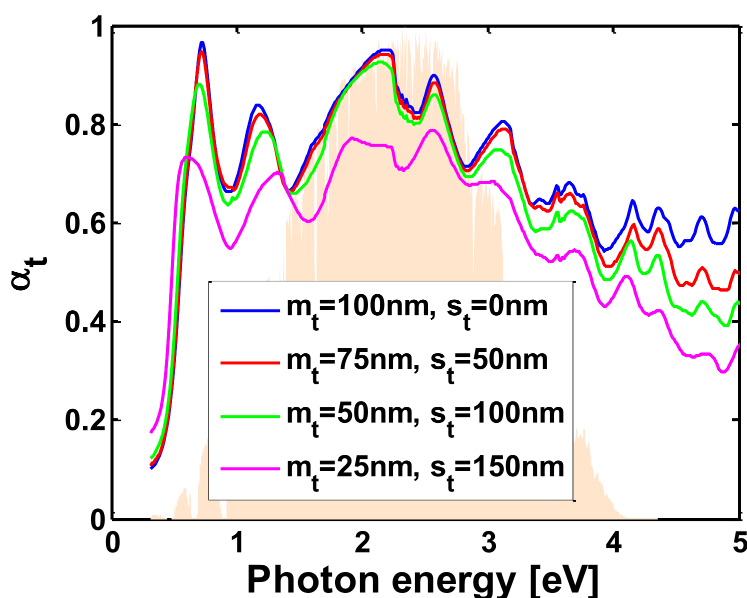

Figure S6. FDTD simulated absorption spectra with varying metal, m_t, and Al_2O_3, s_t, thicknesses. The inner radius, *r*, is held constant. Note that for m_t greater than the skin depth, variations in both m_t and s_t have little impact on the absorption spectrum.